Direct Numerical Simulation of Adverse Pressure Gradient Turbulent Boundary Layer up to $Re_\theta \simeq 8000$

Hussein Rkein, Jean-Philippe Laval*

Univ. Lille, CNRS, ONERA,
Arts et Metiers Institute of Technology, Centrale Lille Institut,
UMR 9014 -LMFL- Laboratoire de Mécanique des Fluides de Lille - Kampé de Fériet,
F-59000, Lille, France

A direct numerical simulation of a moderate adverse pressure gradient turbulent boundary layer flow on a flat plate was performed on a fairly long domain with a Reynolds number from $Re_\theta \simeq 2000$ to $Re_\theta \simeq 8000$. The mean streamwise velocity profile does not exhibit a clear log region even at the highest Reynolds number. The Reynolds stresses exhibit a well defined peak in the outer region which moves away from the wall before to stabilise at a wall distance y of 0.45 boundary layer thickness after evolving over 20 local boundary layer thicknesses. These outer peaks are the consequences of an excess of production over dissipation and they all scale with the shear stress velocity for wall distance $0.2\delta < y < 0.85\delta$. The different terms of the Reynolds stresses equations are analysed in the outer region and the analysis confirms that the leading terms are the same as for a zero pressure gradient turbulent boundary layer except that the production and dissipation are not negligible in the outer region. The most significant contribution of scales smaller than two Taylor scales is on the pressure strain term of the shear stress equation. The probability of the occurrence of small scale vortices conditioned by the presence of an ejection or a sweep shows that the shear stress contained in ejections is associated with the production and transport of near wall vortices away from the wall. The local mean shear generated by the sweeps increases the production of near wall vortices. Lastly, the large scale structures analysed by means of two point correlations of the streamwise fluctuating velocity are shown to be strongly modified by the adverse pressure gradient. The correlation reveals a decoupling between the near wall streaks and the large scale streamwise structures enhanced by the adverse pressure gradient.

* jean-philippe.laval@univ-lille.fr

I. INTRODUCTION

The accurate prediction of a turbulent boundary layer (TBL) remains a significant challenge in many practical problems including the engineering design of vehicles, internal aerodynamics or turbomachinery. In order to better understand the physics of such flows, it is natural to first concentrate on flat plate zero pressure gradient (ZPG) TBL. However, ZPG conditions are nearly never encountered in real-life applications as the majority of flow problems encounter the effect of complex pressure gradient on flat or curved walls. The applicability of the knowledge from ZPG TBLs to decelerating boundary layers is still rather limited. Despite many simulations and experiments on adverse pressure gradient (APG) TBLs, there is still no consensus and clear understanding of the main effects of the magnitude and upstream history of a streamwise adverse pressure gradient on turbulence statistics and the shape of large scale coherent structures. Despite many proposals, no universal velocity and length scale are able to successfully re-scale the turbulence statistics for a wide range of flow parameters. In order to study the effect of these APG flow parameters, a large variety of experimental and numerical data are needed to cover a wide range of pressure gradients and Reynolds numbers. A summary of the most important studies is given in Fig. 1. Each case is plotted in a Rotta Clauser pressure gradient ($\beta = \frac{\delta_1 U_e}{u_\tau^2}\frac{dU_e}{dx}$) and Reynolds number parameter space.

Most of the detailed databases have been obtained for adverse pressure gradient flows in equilibrium (see [1–3]) either for weak pressure gradient or very strong pressure gradient to focus on the condition before or at the edge of separation. One of the first DNS of APG TBL was performed by Skote et al [1] but the two cases are restricted to low Reynolds numbers and weak pressure gradients ($\beta \simeq 0.24$ and ($\beta \simeq 0.65$). Lee & Sung performed DNS with 3 approximately constant pressure gradients for momentum Reynolds numbers Re_θ of the order of 1300 [2]. The evolution of the pressure gradient in the transition region is documented and the Reynolds stress profiles are analysed in the near-equilibrium region. An outer peak of streamwise root mean square velocity fluctuation was observed for the largest pressure gradient case ($\beta \simeq 1.68$) but this peak does not exceed the inner peak. Gungor et al [4] compared APG TBL evolving from a moderate to a strong adverse pressure gradient (small to large defect cases) with ZPG TBLs and channels. The momentum Reynolds number reached in this DNS of non-equilibrium APG TBL is around 5800 in the downstream region where the pressure gradient is $\beta = 40$. The Reynolds stress budget is analysed in the near wall and the outer region. One of the conclusions is that the magnitude of the mean shear appears to be the main reason for the increase, in relative importance, of the outer layer activity in APG TBLs. The authors also conclude that the "big outer-layer structures dominate the inner layer in the large-defect case in a way that the spectra do not exhibit the streak-related inner peak, but the streaks would nonetheless be present".

The numerical simulations with the highest Reynolds can only be reached by LES. A recent wall resolved LES of near equilibrium APG TBL at Reynolds number up to $Re_\theta \simeq 8700$ with mild adverse pressure gradient ($\beta = 1.4$) has been performed by [5]. The self-similarity of the outer region using the Zagarola-Smits and an alternative scaling based on edge velocity and displacement thickness was investigated. A large enough Reynolds number is necessary to decouple the effect of the pressure gradient in the buffer region from the outer region. Marquillie et al [6] have shown that a strong peak of production in the adverse pressure gradient region was due to the strengthening of the near-wall streaks instability [7] but the Reynolds number was too low and the pressure gradient was evolving too rapidly to study the evolution of the peak of turbulent kinetic energy.

The aim of the present work is to generate a new DNS database of APG TBL at a moderate pressure gradient at the highest possible Reynolds number in order to analyse the origin, the evolution and the scaling of the peak of the Reynolds stresses and to analyse how the streamwise large scale structures are affected by the APG. The present DNS of APG TBL is at the largest Reynolds number achieved by DNS for a moderate APG. The APG is strong enough to generate a clear outer peak but is not too strong to preserve a significant wall shear stress and turbulence production in the near wall region. As can be seen in Fig. 1, several experiments are available at higher Reynolds numbers and similar pressure gradients (see [8–10]). The present DNS was designed to have approximately the same APG magnitude as the experiment of Cuvier et al [10] but with a wider range of almost constant β. The fact that the turbulence is documented along all the APG regions allows us to compare the DNS and the experimental case of Cuvier et al which encounter a different history but a similar magnitude of APG.

II. NUMERICAL SIMULATION

A DNS of APG turbulent boundary layer on a flat plate was performed on a fairly large domain with a Reynolds number up to $Re_\theta \sim 8000$. The DNS was simulated using an inlet condition for velocity from a precursor DNS of ZPG TBL at $Re_\theta \sim 2200$ (see [18]). As the ZPG DNS used to generate the inlet conditions was on a smaller domain, the inlet velocity fields have been extrapolated in the normal direction and periodized by a factor of 4 in the spanwise direction. However, to avoid the exact repetition in the results because of the duplication of inlet planes, a spatial-temporal noise of small amplitude was added to the inlet velocity components similar to the numerical

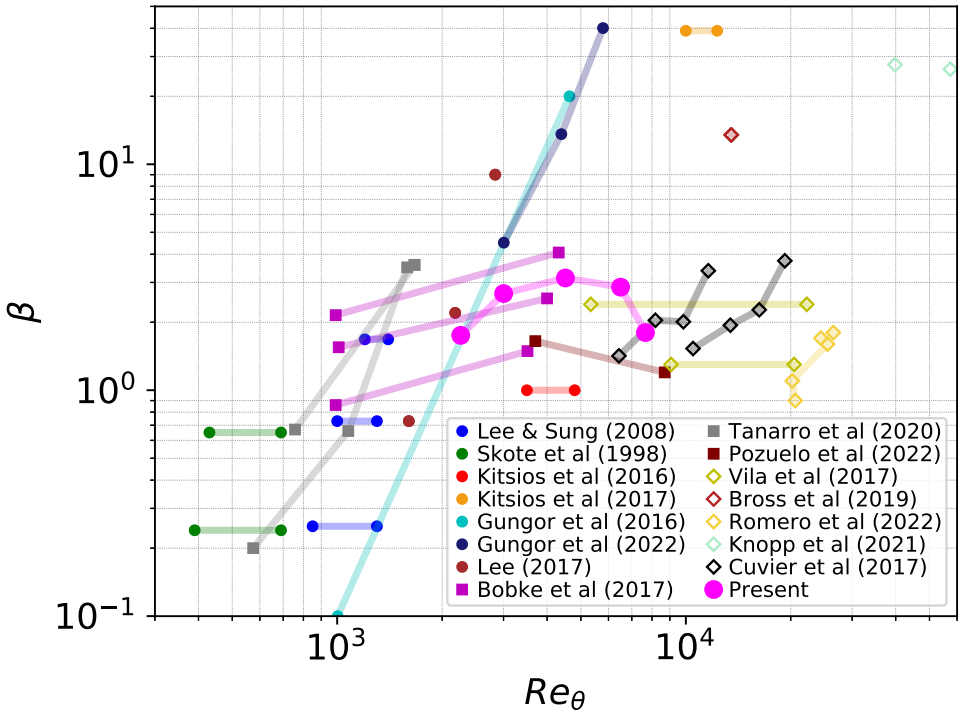

FIG. 1. Summary of the important experimental and numerical studies of turbulent boundary layers in a pressure gradient (β) vs. Reynolds (Re_θ) parameter space [1, 2, 4, 5, 8–17]. The list is not exhaustive and the parameters of each dataset have been extracted from the information of the corresponding papers. The (β, Re_θ) curve is however indicative as the evolution of the two quantities is not always documented. When the (β, Re_θ) range was not available, the case is represented by a single symbol with the parameters at the location at which the statistics are provided. The DNS are indicated with solid circle symbols, the LES with solid square symbols and the experiments with open diamond symbols. Each line corresponds to a single case.

forcing used by Schlatter et al [19]. The temporal and spanwise cutoff scales of the added random signal were fixed at $t_s = 3.7\delta_o/U_e^o$ and $z_s = 0.6$ where δ_o and U_e^o are the boundary layer thickness and the external streamwise velocity at the entrance of the simulation domain. U_e is computed from the mean spanwise vorticity as in Kitsios et al. [3] and the boundary layer thickness is defined as the wall distance at which mean streamwise velocity represents 99% of the external velocity U_e.

In order to generate the adverse pressure gradient, a wall-normal suction velocity has been prescribed at the far-field boundary condition parallel to the wall. This boundary condition has been proposed by Kitsios et al.[3] based on a potential flow solution in an expanding duct and then it was corrected to compensate for the boundary layer growth. The streamwise ($U_{PF} = \partial_y \psi_{PF}$) and wall-normal ($V_{PF} = -\partial_x \psi_{PF}$) components of the potential flow were calculated by derivation of the stream function $\psi_{PF} = Ar^{m+1}sin(\gamma)$ along with the centerline of the duct where the constant A is a scaling parameter, $r^2 = \hat{x}^2 + \hat{y}^2$, m is the exponent of the power law, and $\gamma = (m+1)\arctan(\hat{y}/\hat{x})$, $\hat{x}$ and $\hat{y}$ being the streamwise and wall-normal coordinates respectively (please note that equation (2.2) in Kitsios et al.[3] has a typographic error but other equations defining the boundary conditions in their paper are in fact correct). Then the potential flow coordinates $(\hat{x}, \hat{y})$ are substituted by the DNS coordinates (x, y) using

$$\hat{x} = x - x_o, \text{ and } \hat{y} = y - K(x - x_o) \tag{1}$$

where K is the growth rate of the displacement thickness, and x_o is the virtual origin of the boundary layer which is estimated by extending back the streamline from the inlet boundary layer edge. Finally, the far-field wall-normal boundary condition as a function of the streamwise direction (x) is given as

$$V_\infty(x) = V_{PF}(x - x_o, y_\infty - K(x - x_o)) \tag{2}$$

where the subscript ∞ represents the far-field location. The parameter K is the slope of the increasing curve of the displacement thickness, and the exponent m is obtained by the relationship of m and β proposed by Skote et al.

(1998) [1]. The scaling parameter A is chosen to ensure that the streamwise potential flow velocity at the edge of the boundary layer is coherent with the velocity used in the inlet condition. However, this method does not allow to obtain a perfect constant pressure gradient β along the full simulation domain due to the ZPG TBL inlet which creates a transition region and to the effect of the outlet in the downstream part of the domain. Neumann Boundary conditions are used for the streamwise velocity by imposing a zero spanwise vorticity. A fringe region has been applied on the last 3% of the computational domain in order to force the laminarity of the outgoing flow. For the reason explained earlier, we choose a moderate pressure gradient comparable in magnitude with an APG TBL experiment from [10] on a long ramp in the LMFL wind tunnel at Reynolds number up to $Re_\theta \sim 23000$.

The DNS has been simulated using the open-source code Incompact3D developed by Laizet et al [20]. Sixth-order compact finite difference schemes are used for the spatial discretization and the third-order Adams-Bashforth scheme for the time advancement using a time step $\Delta t^+ = 0.0125$ based on friction velocity at the outlet. The main parameters of the simulation are given in Table I. The simulation is well resolved on the full boundary layer thickness (the normal grid resolution at the top of the TBL Δy^+_δ is of the order of 4.7). This allows us to perform detailed and accurate statistics of both large scales and small dissipative scales. A large database of 100 TB was recorded with the results on 70 characteristic times $T = \delta_{max}/U_e$ after the transient. It is composed of 211 three-dimensional velocity and pressure fields as well as a time evolution (every 1.37 wall unit time) of a 3D restricted domain in the downstream region of the flow ($6818 < Re_\theta < 7582$) and three normal-spanwise planes. A snapshot of the spanwise vorticity in the full simulation domain is shown in Figure 2.

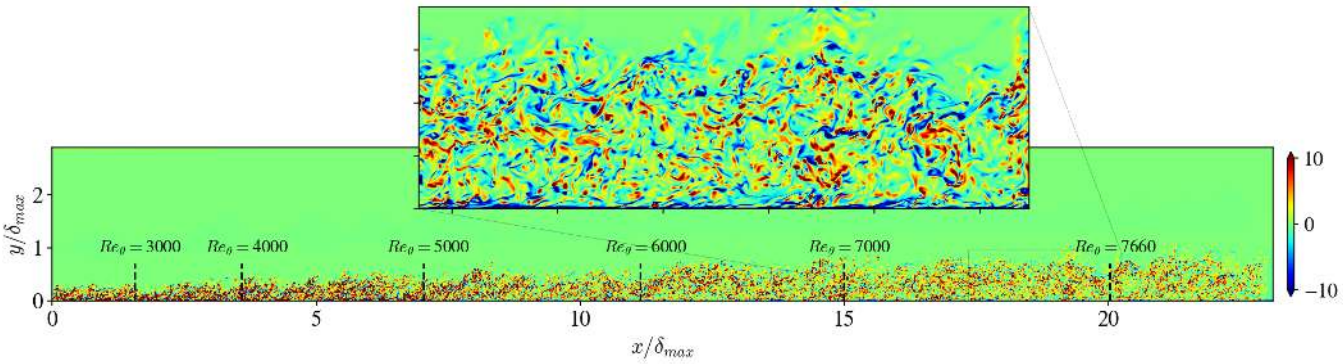

FIG. 2. Snapshot of the spanwise vorticity in a streamwise wall-normal plane on the full simulation domain normalised by δ_{max} and U_e (the maximum boundary layer thickness at the end of the simulation domain (before the fringe region) and the external velocity at this location).

Throughout the paper, the streamwise, wall-normal and spanwise directions are referred to as x, y and z, or 1, 2 and 3 for index notation. The corresponding instantaneous velocity components are $\tilde{u}$, $\tilde{v}$ and $\tilde{w}$. The brackets $\langle\cdot\rangle$ denote ensemble and spanwise averaging. Furthermore, uppercase and lowercase letters denote the mean value and the fluctuations, respectively. Thus $\tilde{u} = \langle\tilde{u}\rangle + u_i = U_i + u_i$.

TABLE I. Parameters of the APG TBL normalised by the quantities (δ_{max}, u_τ) at the outlet. N_x, N_y and N_z are the number of grid points in the streamwise, normal and spanwise directions, L_x, L_y and L_z are the dimensions of the domain and Δx^+, Δy^+, Δz^+ the grid resolution in wall unit (Δy^+_δ being the normal grid size at the top of the boundary layer of size δ_{max}). The range of pressure gradient β and shape factor H are given for the streamwise positions such that $2250 < Re_\theta < 7660$.

Re_θ	$2200 - 8000$
Re_τ	$750 - 1400$
$\beta = \frac{\delta_1 U_e}{u_\tau^2}\frac{dU_e}{dx}$	$[1.8 - 3.3]$
Shape factor H	$[1.43 - 1.83]$
N_x, N_y, N_z	6401, 1025, 1280
L_x, L_y, L_z	$23.3\,\delta_{max},\ 2.9\,\delta_{max},\ 2.33\,\delta_{max}$ $(86.8\,\delta_o,\ 10.8\,\delta_o,\ 8.7\,\delta_o)$
$\Delta x^+,\ \Delta y^+_{min},\ \Delta y^+_\delta,\ \Delta z^+$	5.1, 1.0, 4.7, 2.4

III. REYNOLDS STRESSES

The mean streamwise velocity profiles of APG TBL are plotted in Fig. 3 at several streamwise positions and compared with the profiles of ZPG TBL at comparable Reynolds numbers. As already observed, the APG leads to a reduction of the log region and an extension of the wake region as compared to the ZPG case at the same Reynolds (either Re_θ or Re_τ) [21]. A detailed analysis of the log-law scaling using a diagnostic plot indicates that the profiles exhibit no clear plateau but rather a maximum that moves toward the wall for the lowest Reynolds numbers ($Re_\theta < 3000$) and then moves away from the wall like the square root of Re_θ when moving downstream. This peak does not seem to flatten for any Reynolds numbers indicating that no log region can be identified even at $Re_\theta > 7000$.

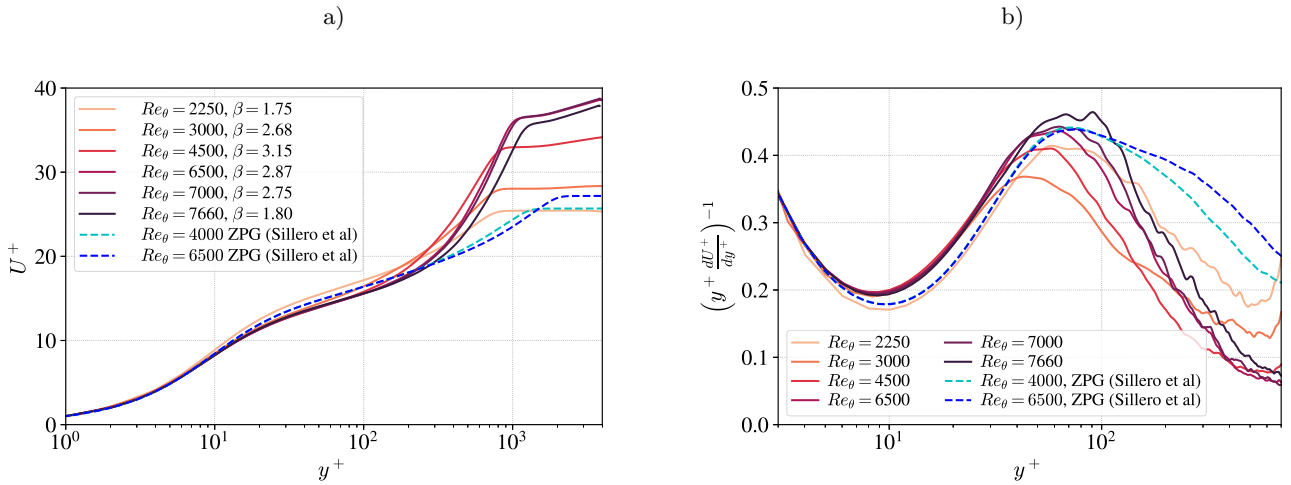

FIG. 3. Evolution of the mean velocity profiles at several streamwise positions (a) and the equivalent diagnostic plots to visualise the "log" region (b). The statistics from ZPG TBL of Sillero et al [22] at $Re_\theta = 4000$ ($Re_\tau = 1307$) and $Re_\theta = 6500$ ($Re_\tau = 2000$) are plotted for comparison.

As already noticed for APG turbulent boundary layers (see e.g. [21, 23]) a second outer peak of the streamwise Reynolds stresses increases with the Reynolds and with pressure gradient to exceed the first inner peak in our case. The inner peak is only weakly affected by the APG as can be seen in Figure 4a) which includes a comparison of Reynolds stresses of zero pressure gradient TBL at equivalent Reynolds numbers. The same behaviour has been observed by Gungor et al [4] with their low deficit (moderate APG) case which is comparable to the present case. It is only with a stronger APG that the outer structures and the reduction of the mean shear starts to significantly affect the turbulence statistics of the inner region. The three normal stresses and the shear stress components are presented in Figure 4. The position of the outer peak seems to evolve identically when moving downstream which indicates a common physics for all velocity components. The magnitude of the outer peaks of each Reynolds stresses increases and stabilises at the streamwise location at which $Re_\theta > 6500$. Lozano et al [24] have hypothesised that the wall is not the element that organises the momentum-carrying eddies in wall turbulence, whose intensities and sizes are controlled instead by the mean production rate of turbulent kinetic energy with no explicit reference to the distance to the wall. As a consequence, they proposed a characteristic velocity scale based on the shear stress $u^* = \sqrt{-\langle uv \rangle}$ and tested this scaling on channel flows with different mean velocity profiles obtained by different boundary conditions. In the present results of APG TBL, the Reynolds stress profiles normalised by the shear stress velocity u^* are constant for wall distances $0.15 < y/\delta < 0.8$ and for all streamwise positions. These constant values 2, 1.3 and 1.8 for the streamwise, wall-normal and spanwise Reynolds stresses respectively are the same as for zero pressure gradient TBL of Sillero et al [22] at similar Reynolds numbers (not shown).

In order to understand the physics associated with the growth of the outer peak, the Reynolds stress tensor budget has been computed along the full simulation domain. Starting from the Navier-Stokes equations, the Reynolds stress transport equations can be obtained in the form

$$\frac{\partial \langle u_i u_j \rangle}{\partial t} + U_k \frac{\partial \langle u_i u_j \rangle}{\partial x_k} = P_{ij} + T_{ij} + D_{ij} + D_{\rho,ij} + \Phi_{ij} - \epsilon_{ij} \tag{3}$$

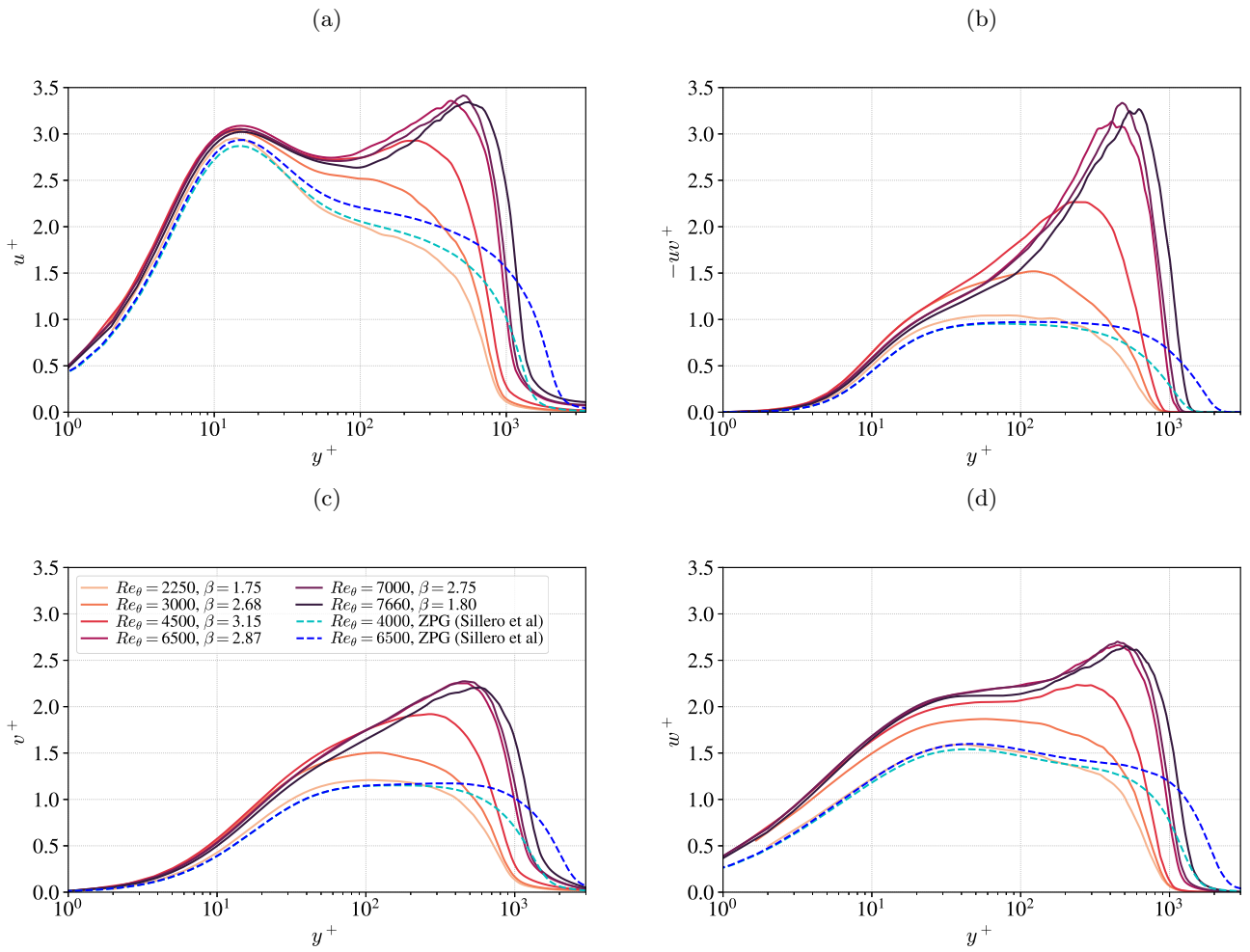

FIG. 4. Reynolds stresses profiles at several streamwise positions. The statistics from ZPG TBL of Sillero et al [22] at $Re_\theta = 4000$ ($Re_\tau = 1307$) and $Re_\theta = 6500$ ($Re_\tau = 2000$) are plotted for comparison.

where the left-hand term is the advection and the right-hand terms are defined as follows:

$$P_{ij} = -\langle u_j u_k \rangle \frac{\partial U_i}{\partial x_k} - \langle u_i u_k \rangle \frac{\partial U_j}{\partial x_k}, \tag{4}$$

$$T_{ij} = -\frac{\partial \langle u_i u_j u_k \rangle}{\partial x_k}, \tag{5}$$

$$D_{ij} = \nu \frac{\partial^2 \langle u_i u_j \rangle}{\partial x_k \partial x_k}, \tag{6}$$

$$D_{\rho,ij} = -\frac{1}{\rho}\left(\frac{\partial \langle u_j p \rangle}{\partial x_i} + \frac{\partial \langle u_i p \rangle}{\partial x_j} \right), \tag{7}$$

$$\Phi_{ij} = \left\langle \frac{p}{\rho}\left(\frac{\partial u_i}{\partial x_j} + \frac{\partial u_j}{\partial x_i} \right) \right\rangle, \tag{8}$$

$$\epsilon_{ij} = 2\nu \left\langle \frac{\partial u_i}{\partial x_k} \frac{\partial u_j}{\partial x_k} \right\rangle. \tag{9}$$

P_{ij} is the production, T_{ij} is the turbulent transport, D_{ij} and $D_{\rho,ij}$ are the viscous and pressure diffusion, Φ_{ij} is the pressure strain and ϵ_{ij} is the dissipation. The budget of the turbulent kinetic energy (TKE) equation $k = \frac{1}{2}\langle u_i u_i \rangle$ is obtained by contracting i and j in the above equations.

The two main components of the turbulent kinetic energy budget (production and dissipation) and their sum (the TKE source) are plotted in Fig. 6 for $3000 < Re_\theta < 7000$. As the production is mainly controlled by $\langle uv \rangle \partial U / \partial y$ the

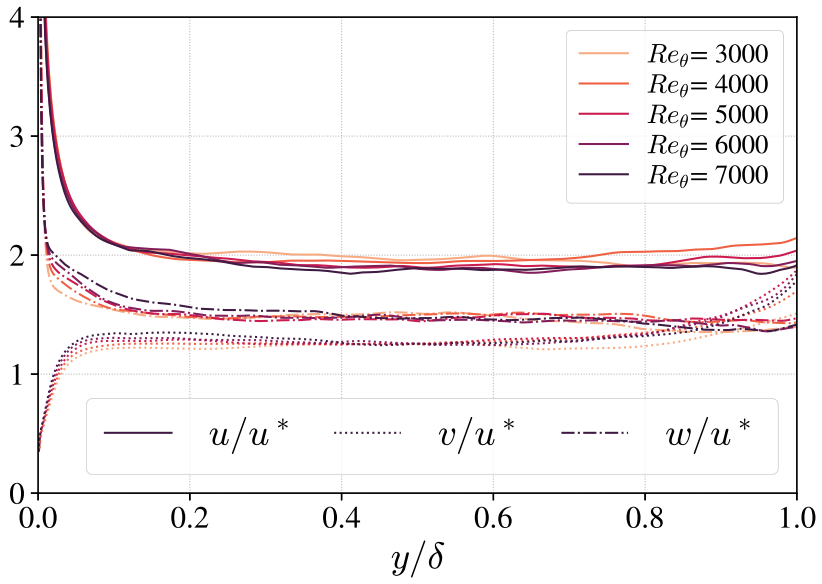

FIG. 5. Mean velocity fluctuation profiles normalised by the shear stress velocity $u^* = \sqrt{-\langle uv \rangle}$ at 5 streamwise positions and Reynolds numbers.

outer peak of the production starts to form at $Re_\theta = 4000$ at the same time as the peak of $\langle uv \rangle$ and other Reynolds stresses components. The emergence of an outer peak of dissipation is delayed to $Re_\theta > 5000$ which corresponds to 7 local boundary layer thicknesses downstream. Further downstream, both production and dissipation exhibit an outer peak but the production always exceeds the dissipation on a wide range of wall distances from 0.2δ to 0.85δ. The source terms (production + dissipation) which supply the outer peak of kinetic energy corresponds to 20% of the production in this range. Due to a slight vertical shift of the production peak ($y \simeq 0.5\delta$) with respect to the dissipation peak ($y \simeq 0.4\delta$), the maximum source peak stabilises near 0.55δ.

As can be seen from the Reynolds stress profiles, the outer peak appears near $y^+ = 100$ at $Re_\theta = 3000$ and moves away from the wall to stabilise before the end of the simulation. For mild APG TBL in equilibrium, the outer peak of turbulence intensity has been located at 1.3 displacement thickness (δ_1) or 0.4 to 0.5 boundary layer thickness (δ) from the wall (see e.g. [3]). In the present case of APG out of equilibrium, the peaks of all Reynolds stresses profiles are shown to evolve similarly to reach this wall distance at a streamwise position of the order of 20 local boundary layer thicknesses defined by $x_\delta(x) = \int_0^x \delta(x')^{-1} dx'$ (see figure 7a) after the start of the adverse pressure gradient ($x = 0$ in our case). This evolution is in accordance with the experimental results of Cuvier et al [10] for a similar APG TBL over a long ramp at higher Reynolds numbers ($Re_\theta \simeq 23000$) although the evolution and magnitude of the pressure gradient are not exactly the same. As the two APG flows do not encounter the same history of pressure gradient which extends over a long domain, on which the boundary layer thickness evolves significantly, the choice of local boundary layer thicknesses to normalise the streamwise position seems more pertinent than the averaged one. The extent of the simulation being larger than the experimental one (based on x_δ), the peaks of Reynolds stresses profiles continue to move away from the wall to stabilise near 1.5 displacement thickness or 0.45 boundary layer thickness despite the fact that the pressure gradient starts to decrease at $x_\delta = 20$. These results show that, for a mild pressure gradient, a minimum of 20 local boundary layer thicknesses is needed for the outer peak position to stabilise even when the pressure gradient does not evolve significantly as in the present DNS case. Even if the streamwise extend to stabilise the peak of the Reynolds stresses observed for these two cases is similar it would be interesting to check if it depends on the intensity of the pressure gradient.

The adverse pressure gradient in a TBL creates an inflectional point in the mean velocity profile. This inflection point has been observed in many experimental and numerical studies [25, 26]. In the large defect case (strong pressure gradient) Schatzman & Thomas [27] and Kitsios et al. [3] invoked the similarity with mixing layers (see also [28]). It has been shown that the position of the outer peaks of the Reynolds stresses in APG flows is very close to the most external inflection point of the mean velocity profile (see [25], [29],[30]). However, Maciel et al [31] reported some flow regions with small mean velocity defects (corresponding to a shape factor $H < 2$) where the Reynolds stresses

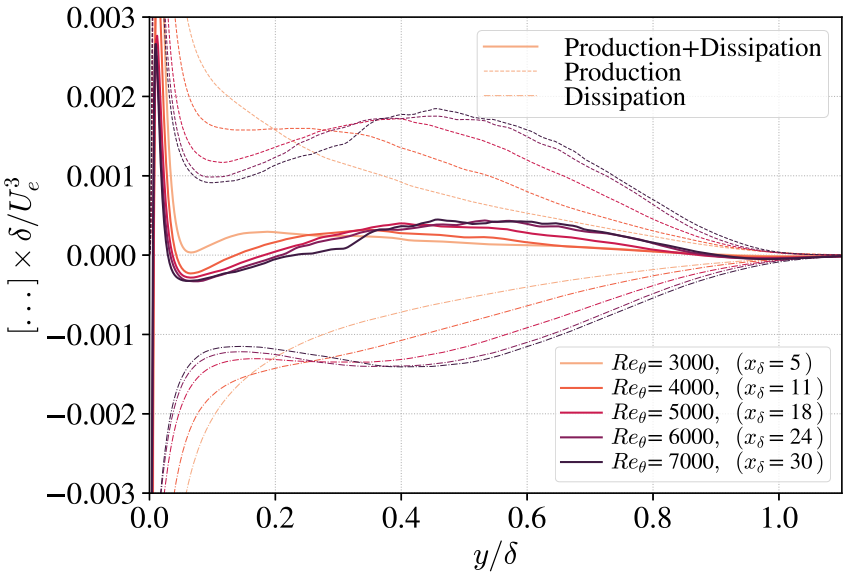

FIG. 6. Production and turbulent dissipation rate of turbulent kinetic energy in outer scaling at several streamwise positions (the positions $x_\delta = \int_0^x \delta(x')^{-1} dx'$ in local boundary layer thicknesses are indicated in parentheses).

have an outer maximum while the mean velocity profile does not have an inflection point. In [32], Maciel et al report no evidence for the coherent structures indicative of an inflectional instability and suggest that the inflectional velocity profiles and the outer Reynolds stress peaks could be simply correlated, without sharing a cause-and-effect relationship. Schatzman & Thomas proposed new length and velocity scales, based on the shear and velocity at the inflection point [27]. This embedded shear layer scaling was tested by Balantrapu et al [28] in a highly decelerated axisymmetric turbulent boundary layer. In the present case with moderate pressure gradient ($H < 1.82$), the mean velocity gradient being almost constant in a wide range of wall distance, this inflection point is not well defined and it is not possible to conclude that it coincides with the normal position of the Reynolds stresses outer peak. The scaling proposed by Schatzman & Thomas was investigated but the uncertainty on the position of the inflection point leads to a very large uncertainty on the length and velocity scales.

We now analyse in more detail the kinetic energy budget and the Reynolds stress budget at the streamwise position $x \simeq 32\delta_{loc}$ ($Re_\theta \simeq 7000$) which corresponds to the largest Reynolds number such as the APG is still significant (β of the order of 3) before to drop. The different terms of the kinetic energy budget and the Reynolds shear stress budget are shown in Figures 8 and 9. As for the ZPG TBL of Sillero et al at a similar Reynolds number [22], the kinetic energy budget in the outer region is dominated by the production and dissipation terms which are however larger than in the ZPG case. The presence of an outer peak of production also leads to a significant negative peak of turbulent transport surrounded by two positive peaks. The picture for the Reynolds shear stress is simpler as the budget is dominated by a positive pressure strain term compensated by a negative production of $\langle uv \rangle$ (mainly $-v^2 \partial U/\partial y$).

It has been shown in Figs. 4 and 5 that all the Reynolds stress components evolve simultaneously in the outer region and exhibit the same peak at the same y position which leads to constant profiles over a large wall distance when normalised with the shear stress velocity profile u^*. As for the ZPG case, the production and pressure strain terms are responsible for the transfer between the normal components of the Reynolds stresses and the shear stress and governs the inter-component energy transfer. The leading terms (production, dissipation and pressure strain) of each component of the Reynolds stress budget in the outer region are compared in Fig. 10a). The shear stress and $\langle v^2 \rangle$ are linked by the production term $-\langle v^2 \rangle \partial U/\partial y$ and $-\langle uv \rangle \partial U/\partial y$ is the mean production term for $\langle u^2 \rangle$. As for the ZPG case, the evolution of the normal and spanwise Reynolds stresses is dominated by the pressure strain and dissipative terms. The pressure strain of $\langle uv \rangle$ is of the same order as the pressure strain of $\langle u^2 \rangle$ and approximately twice the same term for $\langle v^2 \rangle$ and $\langle w^2 \rangle$. The 2D spectra of the pressure strain have been analysed by Gungor et al [4]. They conclude that the 2D spectra have similar features in the outer regions of flows with a different pressure gradient, such as shape and wavelength aspect ratios, as well as relative sizes between energy, production and pressure-strain

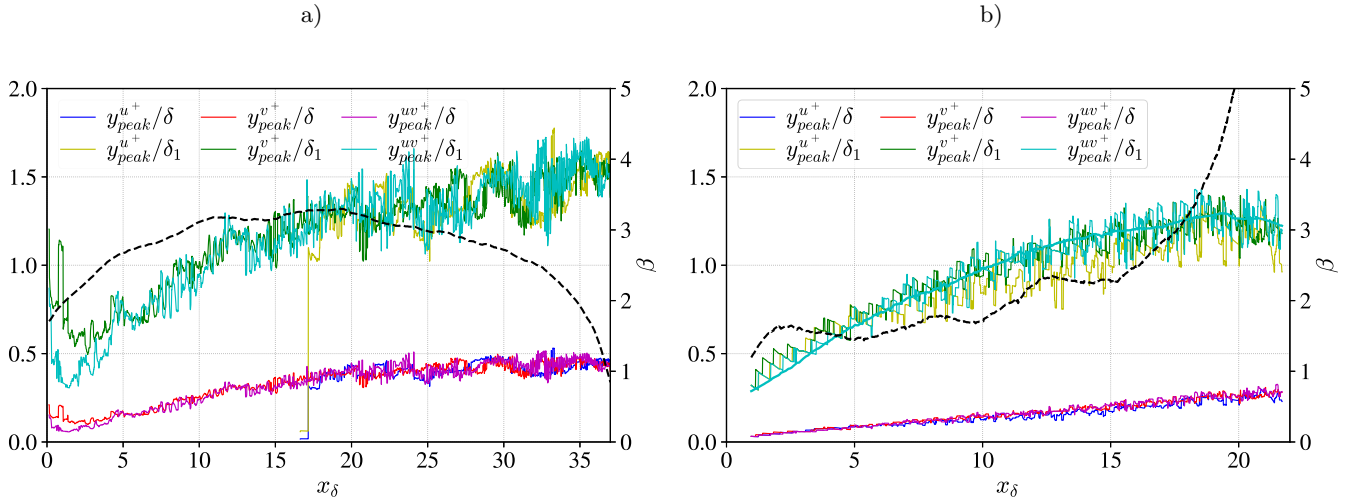

FIG. 7. Evolution of outer peak wall normal position of the Reynolds stresses with respect to the boundary layer thickness (δ) and the displacement thickness (δ_1) for the present DNS of APG TBL (left) and the experimental results of a TBL flow ($Re_\theta = 23000$) over a ramp (right) at $-5°$ from [10] with comparable magnitude (although different evolution of adverse pressure gradient $\beta = \frac{\delta_1 U_e}{u_\tau^2}\frac{dU_e}{dx}$ plotted with dash lines, right axis). x_δ is the position in local boundary layer thicknesses from the start of the APG ($x = 0$).

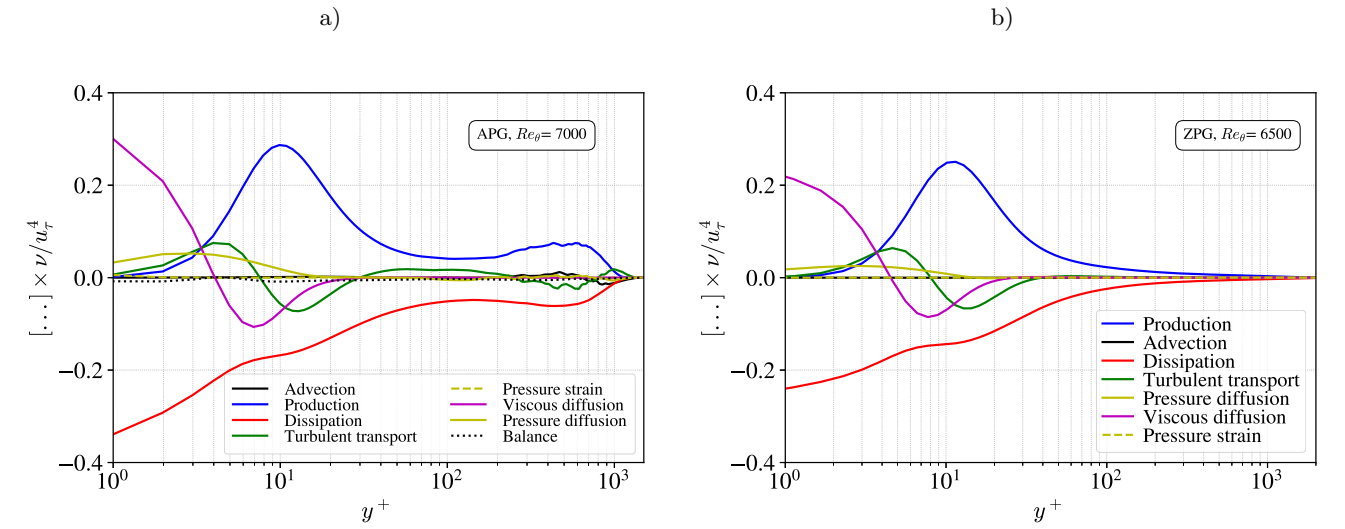

FIG. 8. Kinetic energy budget for the present APG TBL case at the streamwise position x such that $Re_\theta \simeq 7000$. ($Re_\tau = 1120$) (a) and for the ZPG TBL case of Sillero et al [22] at $Re_\theta \simeq 6500$ ($Re_\tau = 2000$).

structures.

In order to distinguish between the contribution of small scales and large scales on each leading term of the Reynolds stress budget, the same terms have been computed from the large scales $\overline{\mathbf{u}}$ and $\overline{p}$ obtained by a streamwise-spanwise 2D least square 3rd order spline filter of the original velocity and pressure fields using the LSQBivariateSpline routine from Scipy which is based on the fitpack library [33]. This filtering was selected for its locality in space and the sharpness of its transfer function (see [34] for more details about the property of this filter). The filter width, which corresponds to the spacing of the knots used for the 3rd order splines, is of the order of 100 wall units in x and z (corresponding to 0.09δ, or approximately two Taylor scales λ at $y/\delta = 0.5$). The filter width was chosen to filter out the small scales vortices smaller than 2λ in order to highlight their contribution in the Reynolds stress budget. When comparing the terms computed with the large scales only in Fig. 10b with the terms computed with all scales, i.e. without filtering (Fig. 10a), the most affected term is the pressure strain of $\langle uv \rangle$ which is divided by a factor of two when the three other pressure strain terms remain almost unchanged. The effect is similar to the production terms

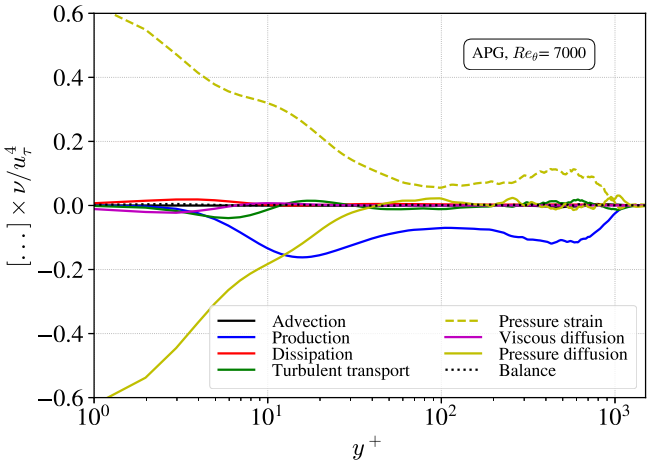

FIG. 9. Reynolds shear stress budget for the present APG case at the streamwise position x such that $Re_\theta \simeq 7000$.

as only the production term of $\langle uv \rangle$ (i.e. $\langle v^2 \rangle \partial U/\partial y$) is significantly reduced when computed with the large scales. These results indicate an important contribution in the outer layer of small scales into the two leading terms of the shear stress equation.

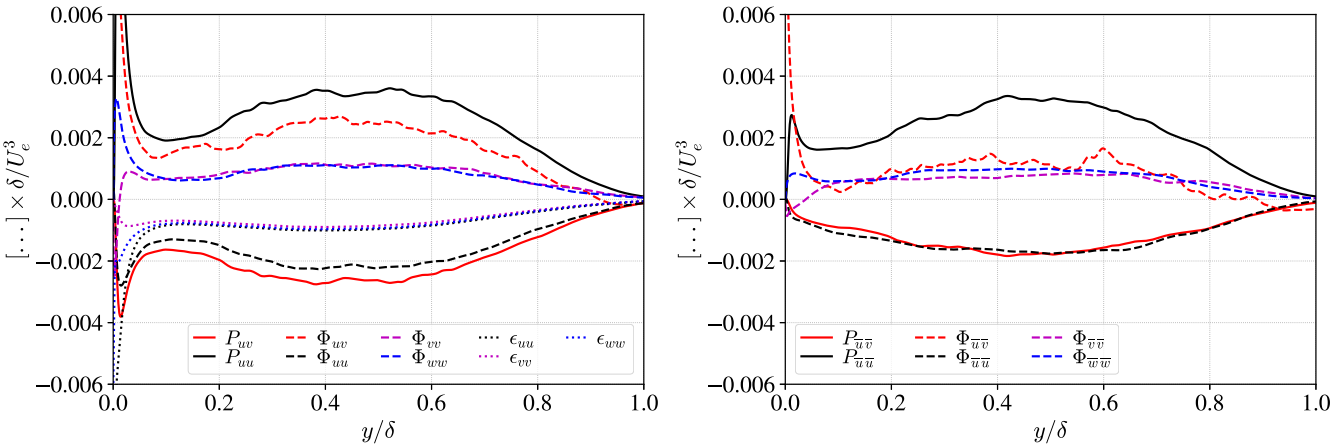

FIG. 10. Leading production (P_{ij}), pressure stain (Φ_{ij}), and dissipation (ϵ_{ij}) terms of the Reynolds stress equations at $Re_\theta \simeq 7000$; (a) Terms computed with all scales, (b) same terms computed with the largest scales $\overline{\mathbf{u}}$ obtained by applying a 3rd order 2D (streamwise spanwise) least square spline filter with a filter width of approximately $100^+ \times 100^+$ corresponding to the nodes spacing for the least square spline (see [34] for the transfer function of the filter). The statistics are computed with the 1315 velocity fields saved on a restricted domain (recorded every 1.37 wall unit time).

The smallest scales in turbulence are usually associated with small scale vortices. In order to make the link between the ejection and sweep, which are the main components of the shear stress, and the small scales, the two point correlations between the ejections (respectively sweeps) and the intense vortices, defined as the location where the Q-criterion (based on the second invariant of the velocity gradient tensor) is larger than a given positive value, have been evaluated and plotted in Fig. 11 (respectively Fig. 12). The ejections (respectively sweeps) are defined as the regions where $-uv > 1.75\,\sigma_u(x_o, y_o)\,\sigma_v(x_o, y_o)$ and $u < 0$ (respectively $u > 0$), $\sigma_u(x_o, y_o)$ and $\sigma_v(x_o, y_o)$ being the standard deviation of u and v at the fixed point (x_o, y_o). The probability of having a vortex is increased by a factor of two in a region downstream and above an ejection and reduced below an ejection near the wall for all y_o positions of the ejection. The second column of Fig. 11 demonstrates that this higher probability of having a vortex in a region

downstream and above an ejection is mainly linked to the presence of an ejection and much less associated with the presence of a low speed streaks. The correlation conditioned by a sweep is rather different. A significant increase in the probability of having a vortex around a sweep is observed with a higher probability upstream and slightly below the sweep. This increase is also observed when conditioned by a high speed streak but with a lower magnitude and restricted to a region below the fixed point. These results illustrate the fact that the shear stress contained in ejections is associated with the production and transport of near wall vortices away from the wall and the local mean shear generated by the sweeps and to a lesser extent by the high speed streaks increases the production of near wall vortices.

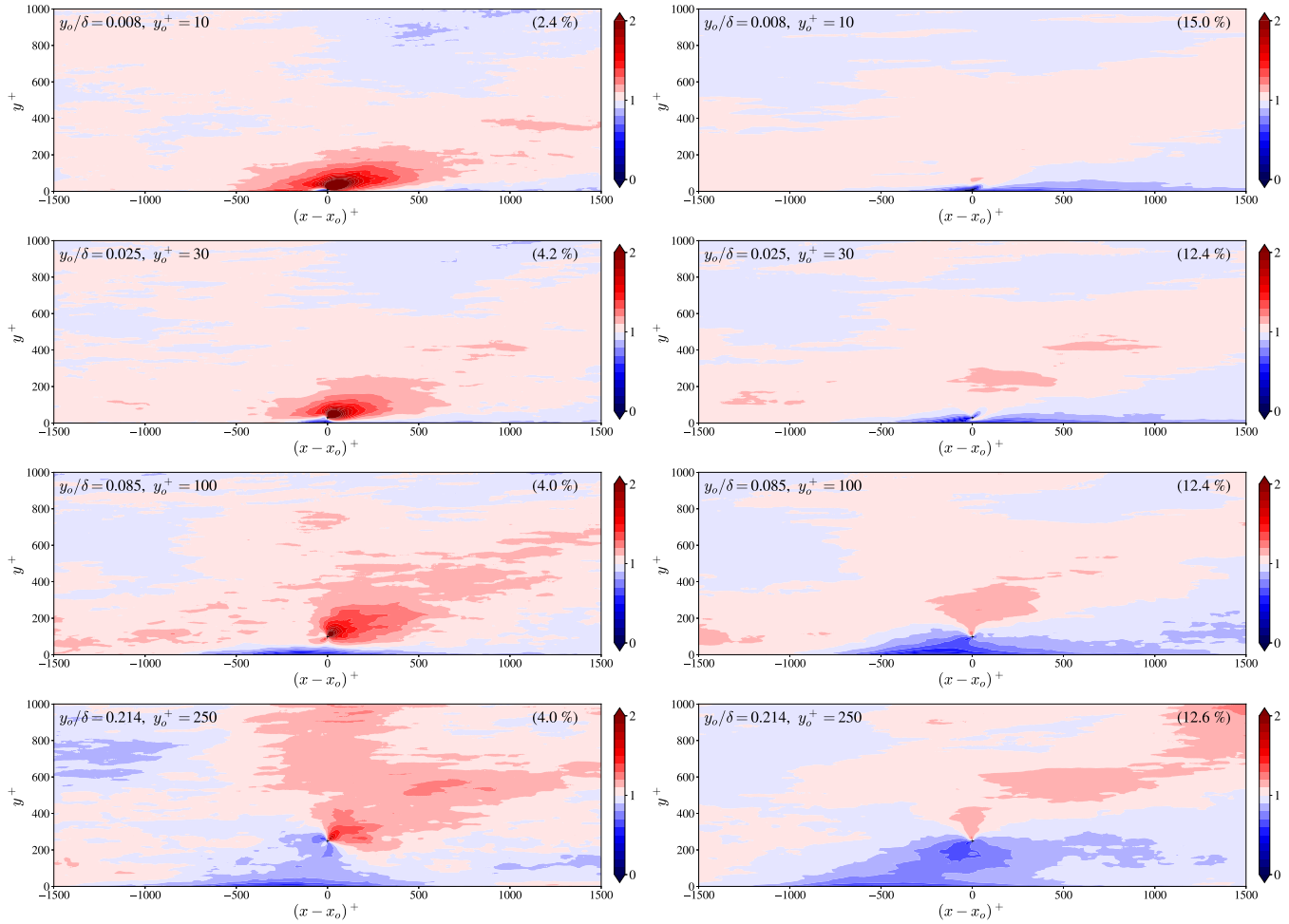

FIG. 11. **Left**: Probability of being inside a vortex (defined as $Q > 0.03$) conditioned by an ejection ($-uv > 1.75\,\sigma_u(x_o, y_o)\,\sigma_v(x_o, y_o)$ and $u < 0$) at the fixed point (x_o, y_o) normalised by the probability of being inside a vortex without condition at a fixed point. **Right**: Probability of being inside a vortex ($Q > 0.03$) conditioned by a low speed streak which is not part of an ejection ($u < -\sigma_u(x_o, y_o)$ and $-uv < 1.75\,\sigma_u(x_o, y_o)\sigma_v(x_o, y_o)$) at the fixed point. The percentage in the upper right of each plot corresponds to the fraction of the points satisfying the condition at the fixed point. The results are given at the streamwise position x_o such that $Re_\theta \simeq 7000$. The statistics are computed with every other velocity field saved on a restricted domain and averaged in the spanwise direction and over a streamwise distance of 1.5 local boundary layer thickness centered on x_o.

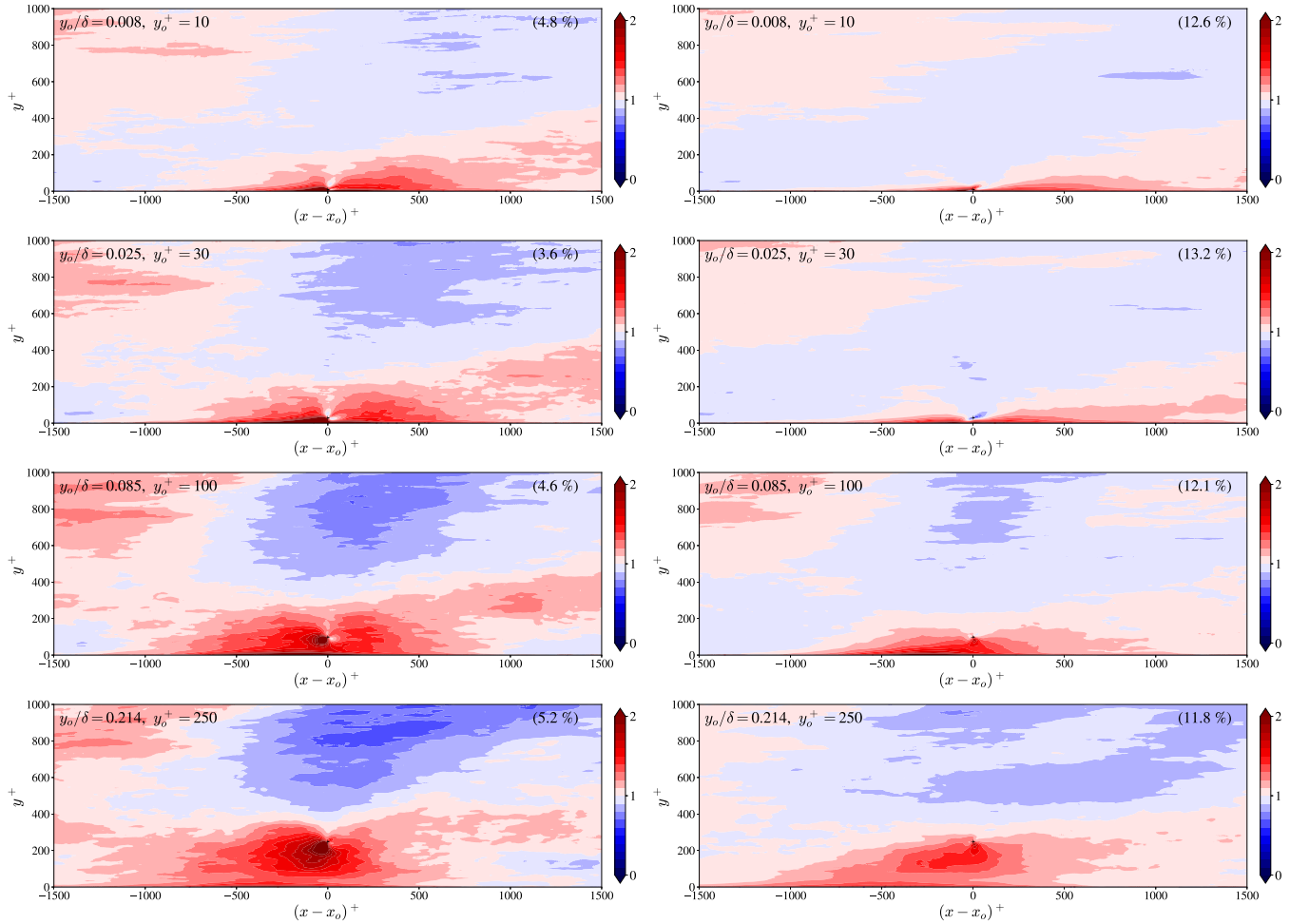

FIG. 12. **Left**: Probability of being inside a vortex (defined as $Q > 0.03$) conditioned by a sweep ($-uv > 1.75\,\sigma_u(x_o, y_o)\,\sigma_v(x_o, y_o)$ and $u > 0$) at the fixed point (x_o, y_o) normalised by the probability of being inside a vortex without condition at a fixed point. **Right**: Probability of being inside a vortex ($Q > 0.03$) conditioned by a high speed streak which is not part of a sweep ($u > \sigma_u(x_o, y_o)$ and $-uv < 1.75\,\sigma_u(x_o, y_o)\sigma_v(x_o, y_o)$) at the fixed point. The percentage in the upper right of each plot corresponds to the fraction of the points satisfying the condition at the fixed point. The results are given at the streamwise position x_o such that $Re_\theta \simeq 7000$. The statistics are computed with every other velocity field saved on a restricted domain and averaged in the spanwise direction and over a streamwise distance of 1.5 local boundary layer thickness centered on x_o.

IV. LARGE SCALE STRUCTURES

The increase of the outer peak of turbulence intensity in large Reynolds number ZPG TBL is associated with the presence of large scale structures of the streamwise fluctuating velocity. Lee [13] has shown that the streamwise coherence of the u'-structures was increased for mild APG and reduced for stronger APG compared to ZPG TBL. They attribute the increase of the streamwise length scale for the large-scale u′-structures to the more active merging event between adjacent u'-structures induced by the increased spanwise length scale of the structures for the APG flows. These structures can be decomposed on wall attached structures (self-similar or not depending on their height l_y with respect to 0.6δ) and wall detached ones (see [35, 36]). From their study at moderate APG ($\beta \simeq 1.43$), Yoon et al [36] have shown that the attached self-similar structures could be more universal wall motions in the logarithmic region not strongly affected by a pressure gradient and the non-self-similar are responsible for the strong increase of the outer peak. Such a decomposition of large scale structures requires a large database with sufficient uncorrelated fields which was not possible for the present study at a larger Reynolds number.

However, in order to further investigate the large-scale motions, the coherent structures of streamwise fluctuating velocity have been detected separately in space. Different methods have been proposed for such detection. Solak and Laval [18] used a simple thresholding technique to detect the structures of the streamwise velocity fluctuation where the threshold was chosen as the standard deviation of streamwise velocity fluctuation at $y^+ = 100$ to retain a large fraction of the kinetic energy. Yoon et al. [36] detected the same type of coherent structures from a DNS of APG TBL ($\beta = 1.43$) using a threshold variable with the wall-normal distance. Other methods have been used in the literature to detect different types of coherent structures [16, 37]. Binary images $\mathbb{B}^{\ominus}$ and $\mathbb{B}^{\oplus}$ indicative of negative and positive streamwise fluctuations are obtained respectively by,

$$\mathbb{B}^{\ominus} = \begin{cases} 1 & \text{if } u' < C_{thr}\,\sigma_u^{100^+} \\ 0 & \text{otherwise} \end{cases} \tag{10a}$$

$$\mathbb{B}^{\oplus} = \begin{cases} 1 & \text{if } u' > C_{thr}\,\sigma_u^{100^+} \\ 0 & \text{otherwise} \end{cases} \tag{10b}$$

where $\sigma_u^{100^+}$ is the standard deviation of the streamwise velocity at $y^+ = 100$, and C_{thr} is the threshold parameter which was set to 1. The same reference velocity $\sigma_u^{100^+}$ has been used as in the ZPG case of Solak and Laval [18]. In the ZPG case, $y^+ = 100$ corresponds approximately to the beginning of the plateau or the smooth peak which is observed in the outer region of the boundary layer at high Reynolds numbers. In our APG case, the corresponding threshold is located at the crest between the inner and outer peaks of the streamwise velocity fluctuation and it is always smaller than the intensity of the outer peak which is related to the large-scale motions. The volume fraction, momentum and kinetic energy retained for each type of structure are given in Table II. The volume fraction of the two types of structures and the kinetic energy of the low speed ones remain almost unchanged but the kinetic energy of the high-speed streamwise structures is increased from 34% to 43% by the effect of APG. This observation is in agreement with the results of Ganapathisubramani et al. [38] where an analysis of the small-scale streamwise velocity fluctuations conditioned on high- and low-momentum shows that low-speed quantities dominate the high-speed ones far from the wall.

TABLE II. Streamwise energy, momentum and volume fraction inside the detected structures from eq. (10) in the present APG case ($Re_\theta \simeq 7200$) and ZPG cases of Solak et al. [18] ($Re_\theta \simeq 2000$).

Cases	Energy		Momentum		Volume	
	$\oplus$	$\ominus$	$\oplus$	$\ominus$	$\oplus$	$\ominus$
ZPG	34%	43%	26%	31%	13%	14%
APG	43%	41%	33%	31%	13%	12%

Another statistic to study the effect of the APG on the streamwise large scale structures is the two-point correlations of streamwise velocity fluctuations. The results for the current APG TBL have been compared with the DNS results of a ZPG TBL at a lower Reynolds number (see Figure 13). The effect of APG is shown to increase the inclination and size of the large scale structures. Moreover, the shape of the correlation function in the buffer layer upstream of the fixed point indicates a different organisation in this region with respect to the ZPG TBL. When the fixed point is just above the inner peak of u ($y_o^+ > 50$) associated with near-wall streaks the iso-contours extend much more upstream

of the position x_o of the fixed point and the near-wall part of the iso-contours linked to the near-wall streaks clearly detached from the upper part of the structures (associated with the outer peak of u). The iso-contours also extend further downstream and away from the wall to reach 0.8δ. In Figure 14, the two-point correlation function of the streamwise velocity fluctuation conditioned by the sign of $u(x_o, y_o)$ and normalised by u_τ at the fixed point is plotted for different altitudes y_o of the fixed point. These results reveal the different behaviours with high-speed large-scale structures (when conditioned by $u(x_o, y_o) > 0$) which extends more downstream for $y_o < 100^+$ and more upstream for $y_o > 100^+$. As both conditioned correlations are normalised by u_τ the highest iso-contours show that the variance of positive u is larger than the variance in the negative one for all wall distances y_o. More detailed statistics of each individual structure would be needed to better assess the effect of APG on these large scale structures. However, such statistics would require many more uncorrelated velocity fields than available for the current DNS database.

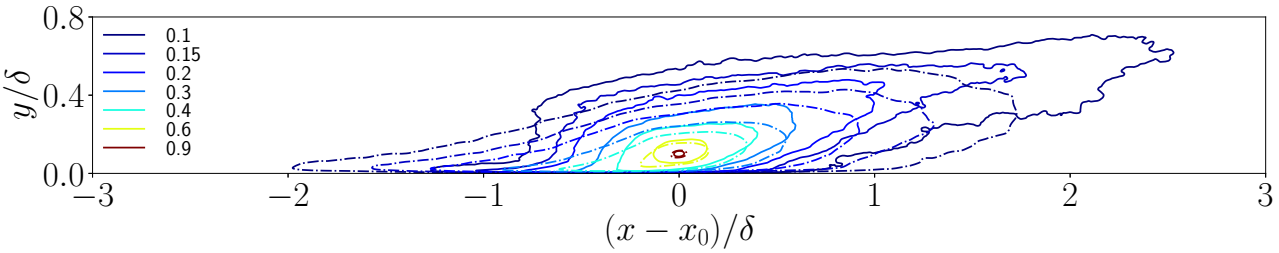

FIG. 13. Comparison of the iso-contours of the two-point correlation of the streamwise velocity fluctuation at $y_o = 0.08\delta$ between the present APG case at $Re_\theta = 7240$ (continuous lines) and the ZPG case at $Re_\theta = 2068$ (dash-dotted lines) from [18]. The correlation is normalised by $\sigma_u(x_o, y_o)$ at the fixed point.

V. CONCLUSIONS

A new DNS of APG TBL over a flat plate has been presented. This simulation is long enough to study the evolution of the Reynolds stress profiles and to follow the growth and stabilisation of the outer peak. This outer peak is located at the same position for all Reynolds stresses and takes more than 20 local boundary layer thicknesses to stabilise at a wall distance of 1.3 boundary layer displacement thicknesses or 0.45δ. The Reynolds stress profiles scale almost perfectly with the shear stress velocity profiles u^* on a wide range of wall distances from 0.2δ up to 0.8δ, independently of the Reynolds numbers (streamwise position in the TBL). The Reynolds stress budget shows that, for this moderate adverse pressure gradient, the leading terms of the equation are the same as for a ZPG turbulent boundary layer. However, the main difference is a significant production and dissipation in the outer region. The pressure strain which is responsible for the energy exchange between the three components and therefore the similarity of the Reynolds stress profiles in the outer region is twice bigger for u^2 and uv than for v^2 and w^2. We have also shown that part of the pressure strain of uv is due to small scales when the pressure strain for the three normal components of Reynolds stresses is more controlled by the large scales (scales larger than 100 wall units or two Taylor scales). The correlation between small scale vortices and the ejection/sweep which play a major role in kinetic energy production shows a preferable concentration of small scales vortices upstream and slightly below a sweep and downstream and above an ejection.

The two point correlations of streamwise velocity fluctuations show a strong effect of APG on the upstream part of streamwise fluctuating velocity inclined structures as compared to the ZPG case and this effect is enhanced for high speed structures. The size and intensity of low and high speed structures are also different, especially for the case where the fixed point of the two points correlation is close to the wall. It is however difficult to compare the size of these large scale structures of streamwise fluctuating velocity with the case of ZPG as their size is strongly related to their kinetic energy which is significantly increased in the outer region and therefore to the choice or normalisation of the two points correlation. More detailed and accurate statistics to discriminate between attached and detached structures would require larger databases which is difficult to obtain by DNS.

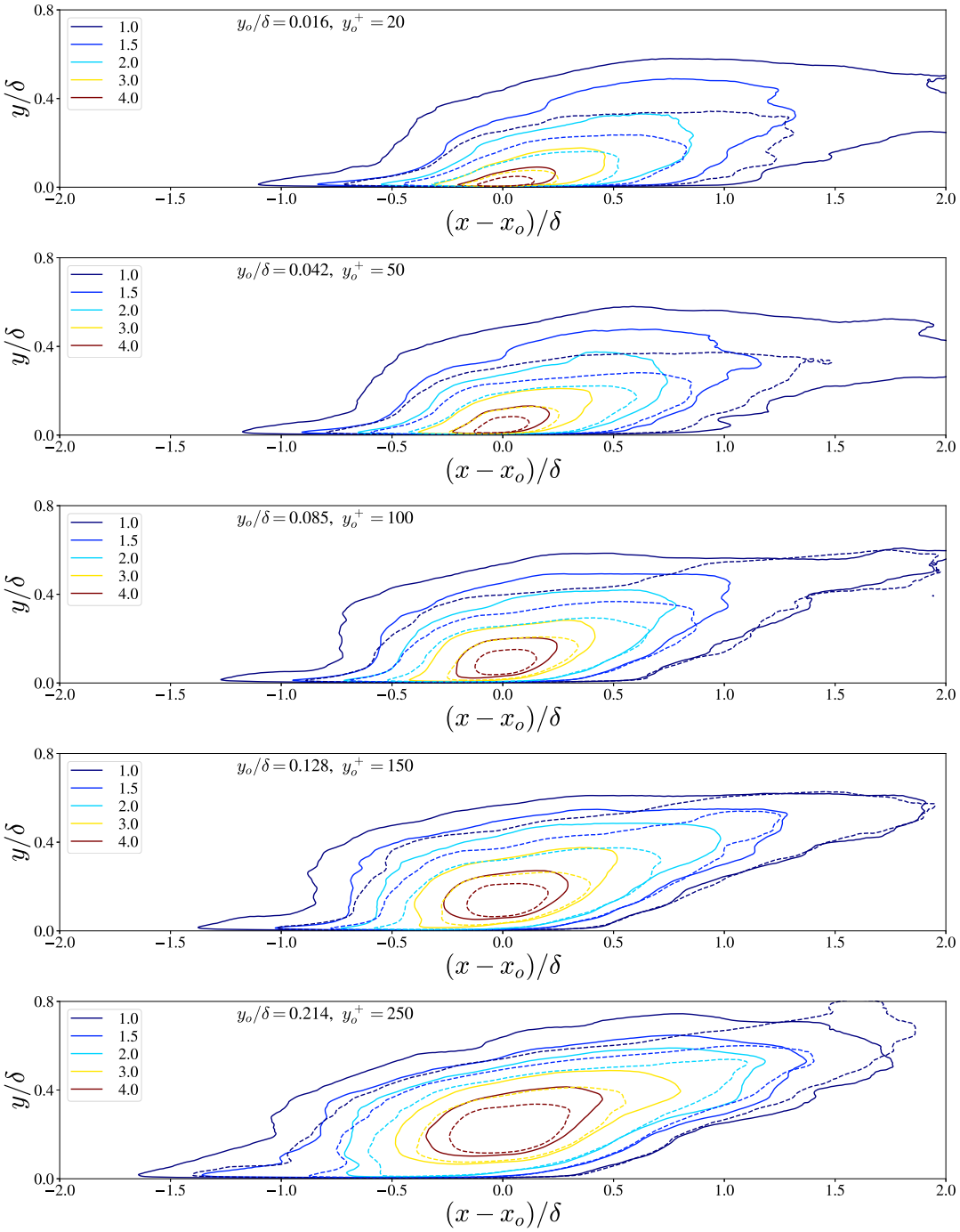

FIG. 14. Iso-contours of the two-point correlations of the streamwise velocity fluctuation u conditioned by $u(x_o, y_o) > 0$ (continuous lines) and $u(x_o, y_o) < 0$ (dash lines) for APG case at x_o such that $Re_\theta(x_o) = 7240$. The correlations are normalised by u_τ^2 at the fixed point (x_o, y_o). The statistics are computed with every other velocity field saved on a restricted domain and averaged in the spanwise direction and over a streamwise distance 1.5 local boundary layer thickness centered on x_o.

ACKNOWLEDGEMENT

This work was supported by the European Community, the French Ministry for Higher Education and Research and the Hauts de France Regional Council in connection with CNRS Research Foundation on Ground Transport and Mobility as part of the ELSAT2020 project. The work was granted access to the HPC resources of IDRIS under the allocation 021741 made by GENCI (Grand Equipment National de Calcul Intensif).

[1] M. Skote, D. S. Henningson, R. Henkes, Direct numerical simulation of self-similar turbulent boundary layers in adverse pressure gradients, Flow, Turbulence and Combustion 60 (1998) 47–85.
[2] J.-H. Lee, H. J. Sung, Effects of an adverse pressure gradient on a turbulent boundary layer, Int. J. Heat Fluid Flow 29 (2008) 568–578.
[3] V. Kitsios, A. Sekimono, C. Atkinson, J. Sillero, G. Borrell, A. Gungor, J. Jimenez, J. Soria, Direct numerical simulation of a self-similar adverse pressure gradient turbulent boundary layer at the verge of separation, J. Fluid Mech. 829 (2017) 392–419.
[4] T. Gungor, Y. Maciel, A. Gungor, Energy transfer mechanisms in adverse pressure gradient turbulent boundary layers: production and inter-component redistribution, J. Fluid Mech. 948 (A5) (2022) 1–38.
[5] R. Pozuelo, Q. Li, P. Schlatter, R. Vinuesa, An adverse-pressure-gradient turbulent boundary layer with nearly constant $\beta \simeq 1.4$ up to $Re_\theta \simeq 8700$, J. Fluid Mech. 939 (A34) (2022) 1–36.
[6] M. Marquillie, U. Ehrenstein, J.-P. Laval, Instability of streaks in wall turbulence with adverse pressure gradient, J. Fluid Mech. 681 (2011) 205–240.
[7] J.-P. Laval, M. Marquillie, U. Ehrenstein, On the relation between kinetic energy production in adverse-pressure gradient wall turbulence and streak instability, Journal of Turbulence 13 (21) (2012) 1–19.
[8] C. Vilas, R. Orlu, R. Vinuesa, P. Schlatter, A. Ianiro, S. Discetti, Adverse-pressure-gradient effects on turbulent boundary layers: Statistics and flow-field organization, Flow Turbulence Combust. 99 (2017) 589–612.
[9] S. Romero, S. Zimmerman, J. Philipp, C. White, J. Klewicki, Properties of the inertial sublayer in adverse pressure-gradient turbulent boundary layers, J. Fluid Mech. 937 (A30) (2022) 1–36.
[10] S. Cuvier, S. Srinath, M. Stanislas, J.-M. Foucaut, J.-P. Laval, C. J. Kahler, R. Hain, S. Schamowski, A. Schroder, R. Geisler, J. Agocs, A. Rose, C. Willert, J. Klinner, O. Amili, C. Atkinson, J. Soria, Extensive characterization of a high reynolds number decelerating boundary layer using advanced optical metrology, Journal of Turbulence 18 (10) (2017) 929–972.
[11] V. Kitsios, C. Atkinson, J. Sillero, G. Borrell, A. Gungor, J. Jimenez, J. Soria, Direct numerical simulation of a self-similar adverse pressure gradient turbulent boundary layer, International Journal of Heat and Fluid Flow 61 (2016) 129–136.
[12] A. Gungor, Y. Maciel, M. Simens, J. Soria, Scaling and statistics of large-defect adverse pressure gradient turbulent boundary layers, Int. J. Heat Fluid Flow 59 (2016) 109–124.
[13] J. H. Lee, Large-scale motions in turbulent boundary layers subjected to adverse pressure gradients, J. Fluid Mech. 810 (2017) 323–361.
[14] A. Bobke, R. Vinuesa, R. Orlu, P. Schlatter, History effects and near equilibrium in adverse-pressure-gradient turbulent boundary layers, J. Fluid Mech. 820 (2017) 667–692.
[15] A. Tanarro, R. Vinuesa, P. Schlatter, Effect of adverse pressure gradients on turbulent ing boundary layers, J. Fluid Mech. 883 (A8) (2020) 1–28.
[16] M. Bross, T. Fuchs, C. J. Kähler, Interaction of coherent flow structures in adverse pressure gradient turbulent boundary-layers, J. Fluid Mech. 873 (2019) 287–321.
[17] T. Knopp, N. Reuther, M. Novara, D. Schantz, E. Schülein, A. Schröder, C. Kähler, Experimental analysis of the log law at adverse pressure gradient, J. Fluid Mech. 918 (A17) (2021) 1–32.
[18] I. Solak, J.-P. Laval, Large-scale motions from a direct numerical simulation of a turbulent boundary layer, Phys. Rev. E 98 (2018) 033101.
[19] P. Schlatter, R. Örlü, Turbulent boundary layers at moderate Reynolds numbers: inflow length and tripping effects, J. Fluid. Mech. 710 (2012) 5–34.
[20] S. Laizet, E. Lamballais, High-order compact schemes for incompressible flows: a simple and efficient method with the quasi-spectral accuracy, J. Comp. Phys. 228 (15) (2009) 5989–6015.
[21] P.-Å. Krogstad, P. E. Skåre, Influence of the strong adverse pressure gradient on the turbulent structure in a boundary layer., Phys. Fluids. 7 (8) (1995) 2014–2024.
[22] J. Sillero, J. A. Jiménez, R. D. Moser, One-point statistics for turbulent wall-bounded flows at Reynolds numbers up to $\delta^+ \simeq 2000$, Phys. Fluids 25 (105102) (2013) 1–16.
[23] Z. Harun, J. Monty, R. Mathis, Y. Marusic, Pressure gradient effects on the large-scale structure of turbulent boundary layers, J. Fluid Mech. 715 (2013) 477–498.
[24] A. Lozano-Durán, H. J. Bae, Characteristic scales of townsend's wall attached eddies, J. Fluid Mech. 868 (2019) 698–725.
[25] M. Z. K. Elsberry, J. Loeffler, I. Wygnanski, An experimental study of a boundary layer that is maintained on the verge of separation, J. Fluid Mech. 423 (2000) 227–261.

[26] D. B. DeGraaff, J. K. Eaton, Reynolds-number scaling of the flat-plate turbulent boundary layer., J. Fluid Mech. 422 (2000) 319–346.
[27] D. M. Schatzman, F. O. Thomas, An experimental investigation of an unsteady adverse pressure gradient turbulent boundary layer: embedded shear layer scaling, J. Fluid Mech. 815 (2017) 592–642.
[28] N. A. Balantrapu, C. Hickling, W. Alexander, W. Devenport, The structure of a highly decelerated axisymmetric turbulent boundary layer, J. Fluid Mech. 929 (A9) (2021) 1–38.
[29] S. I. Shah, M. Stanislas, J.-P. Laval, A specific behavior of adverse pressure gradient near wall flows, in: M. Stanislas, J. Jimenez, I. Marusic (Eds.), Progress in wall turbulence : understanding and modelling, ERCOFTAC Series vol 14, Springer, Villeneuve d'Ascq, France, April 21-23, 2010, pp. 257–265.
[30] W. K. George, M. Stanislas, J. P. Laval, New insights into adverse pressure gradient boundary layers, in: M. Oberlack, J. Peinke, A. Talamelli, L. Castillo, M. Hölling (Eds.), Progress in Turbulence and Wind Energy IV, Springer Berlin Heidelberg, Berlin, Heidelberg, 2012, pp. 201–204.
[31] Y. Maciel, T. Wei, A. Gungor, M. Siemens, Outer scales and parameters of adverse-pressure-gradient turbulent boundary layers, J. Fluid Mech. 844 (2018) 5–35.
[32] Y. Maciel, M. Simens, A. Gungor, Coherent structures in a non-equilibrium large-velocity-defect turbulent boundary layer, Flow Turbul. Combust 98 (1) (2017) 1–20.
[33] P. Diercks, Curve and Surface Fitting with Splines, Oxford University Press., 1993.
[34] C. Li, A-priori analysis of LES subgrid-scale models applied to wall turbulence with pressure gradient, Ph.D. thesis, Ecole Centrale de Lille (2013).
[35] J. Hwang, J. Lee, H. Sung, Statistical behaviour of self-similar structures in canonical wall turbulence, J. Fluid Mech. 905 (A6) (2020) 1–24.
[36] M. Yoon, J. Hwang, H. Sung, Wall-attached structures of streamwise velocity fluctuations in an adverse-pressure-gradient turbulent boundary layer, J. Fluid Mech. 885 (A12) (2020) 1–27.
[37] M. Atzori, R. Vinuesa, A. Lozano-Durán, P. Schlatter, Coherent structures in turbulent boundary layers over an airfoil, in: Journal of Physics: Conference Series, Vol. 1522, IOP Publishing, 2020, p. 012020.
[38] B. Ganapathisubramani, N. Hutchins, J. P. Monty, H. Ng, I. Marušić, Near-wall influence of large-scale motions in high reynolds number turbulent boundary layers, in: Sixth International Symposium on Turbulence and Shear Flow Phenomena, Begel House Inc., 2009.